

Point Spread Functions and Deconvolution of Ultrasonic Images

Christoph Dalitz, Regina Pohle-Fröhlich, and Thorsten Michalk

Abstract—This article investigates the restoration of ultrasonic pulse-echo C-scan images by means of deconvolution with a point spread function (PSF). The deconvolution concept from linear system theory (LST) is linked to the wave equation formulation of the imaging process and an analytic formula for the PSF of planar transducers is derived. For this analytic expression, different numerical and analytic approximation schemes for evaluating the PSF are presented. By comparing simulated images with measured C-scan images, we demonstrate that the assumptions of LST in combination with our formula for the PSF are a good model for the pulse-echo imaging process. To reconstruct the object from a C-scan image, we compare different deconvolution schemes: the Wiener filter, the ForWaRD algorithm, and the Richardson-Lucy algorithm. The best results are obtained with the Richardson-Lucy algorithm with total variation regularization. For distances greater or equal twice the near field distance, our experiments show that the numerically computed PSF can be replaced with a simple closed analytic term based on a far field approximation.

Index Terms—point spread function, PSF, deconvolution, Wiener filter, Richardson-Lucy

1 INTRODUCTION

AN unavoidable problem in ultrasonic imaging is that the image is not an exact representation of the object, but is blurred. This severely limits the quality and resolution of an image. As the same problem occurs with optical imaging in microscopy or astronomy, there has been considerable research on improving the image quality by some kind of “inversion” of the imaging process. These inversion schemes model the imaging process as a space-invariant linear system

$$I(x, y) = f(x, y) * g(x, y) \quad (1)$$

where I is the image, f the object, “*” is the two-dimensional convolution operator, and g is a *point spread function* (PSF) describing the imaging system. As the image I is equal to the PSF g for an object $f(x, y) = \delta(x, y)$ (i.e., a point reflector located in the origin), the PSF can also be considered as a spatial “impulse response”. The process of approximately inverting (1) to obtain f is known as *deconvolution*. Much of the research on

deconvolution of ultrasonic images is devoted to *blind deconvolution*, i.e. the case of unknown PSF g , which is to be estimated from the image I [1] [2] [3]. In *non-blind deconvolution*, the image I is not used for computing the PSF, but it is either measured directly from scattering objects approximately representing an “impulse” [4], or it is reconstructed via inverse filtering for special scattering objects [5] [6], or it is theoretically computed from a model of the imaging process [7].

The present article is devoted to non-blind deconvolution of ultrasonic imaging with planar transducers and homogeneous transport media, and it addresses the two main questions in non-blind deconvolution: how to select a deconvolution algorithm that computes f from given I and g , and how to determine the PSF g .

The classic non-blind deconvolution algorithm is the *Wiener filter* [8], which is widely deployed and has been demonstrated to improve the image quality in x-ray radiography [9] and in ultrasonic imaging [7]. It is very attractive because it provides a simple closed analytic formula for directly computing the deconvolution result in a single step, but it has the disadvantage of creating ringing artifacts. These can be especially problematic in ultrasonic imaging because they seem to indicate echoes which are actually not existent. An algorithm that particularly tries to remedy this shortcoming is the ForWaRD algorithm by Neelamani et al. [10]. Whereas Neelamani et al. have tested the ForWaRD algorithm only on artificially blurred images, Zhou et al. have demonstrated its usefulness for the deconvolution of x-ray phase contrast images [11].

In astronomy and microscopy, a different non-blind deconvolution algorithm is usually deployed that was devised by *Richardson* and *Lucy* in [12] [13]. It is an iterative algorithm and thus slower than the Wiener filter, but, unlike the Wiener filter, it does not suffer from introducing artifacts. It has been shown to perform better than the Wiener filter in the comparative study [14]. As the iteration of the original Richardson-Lucy algorithm does not converge, Dey et al. suggested a *total variation regularization*, which circumvents the need to guess the appropriate numbers of iterations beforehand [15].

For computing the PSF in ultrasonic imaging, Rangarajan et al. proposed a numeric scheme for computing

C. Dalitz and R. Pohle-Fröhlich are with the Niederrhein University of Applied Sciences, Institute for Pattern Recognition, Reinarzstr. 49, 47805 Krefeld, Germany. E-mail: christoph.dalitz@hsnr.de
T. Michalk is with GE Sensing & Inspection Technologies GmbH, Robert-Bosch-Str. 3, 50354 Hürth, Germany.

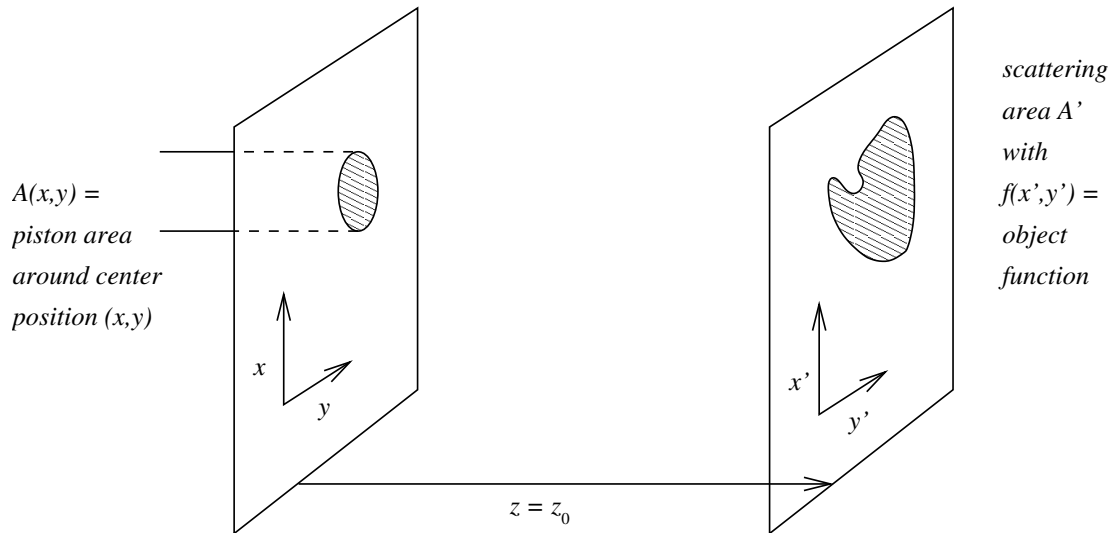


Fig. 1. The geometry of the model and the coordinate systems in the transducer plane and the reflector plane.

the PSF [7]. They did not give an analytic expression for the PSF which the numeric algorithm approximates, but directly derived the numeric scheme with the *patch element method* [16]. Based on Snell's law of refraction [17], they also computed point spread functions in the presence of medium transitions with the patch element method. They used the computed PSFs to restore ultrasonic images with the Wiener filter.

The present article extends the work done by Rangarajan et al. in two ways. The first extension is a derivation of an analytic formula for the PSF by means of comparing a solution of the wave equation with (1) and making a simplifying assumption, which we call the *linear system theory (LST) approximation*. The numeric scheme by Rangarajan et al. turns out to be one special method for computing our analytic expression numerically. Beyond reproducing this earlier result, the analytic expression is useful in itself as a starting point for deriving alternative numeric schemes and also for analytic approximation schemes for computing the PSF, e.g. via a far field approximation that removes the need for numeric integrations when the object is not too close to the transducer. It should be noted that our solution is restricted to planar transducers, because the Rayleigh-integral, on which our solution is based (as explained in the appendix), only holds in this case.

The second extension is a comparison of different convolution algorithms utilizing the PSF, both on simulated and real images. In our experiments, the results of the Wiener filter showed serious artifacts which make it less recommendable for the deconvolution of ultrasonic images. Whereas the results of the ForWaRD algorithm were better than the Wiener filter, the Richardson-Lucy algorithm lead to the best deconvolution results in all cases. To test the assumptions of our model and the LST approximation, we have also compared simulated images with real images, which were in good agreement.

This article is organized as follows: in section 2, we present our physical model and derive the solution for the PSF. The technical parts of the derivation are moved to the appendix to make this section easier to read. In section 3 the different deconvolution algorithms are explained, and in section 4 we present our experimental results for validating our model and for comparing the different deconvolution algorithms.

2 PHYSICAL MODEL AND MATHEMATICAL TREATMENT

Let us consider the following experimental setup for ultrasonic imaging (see Fig. 1):

- A planar transducer is positioned in the transducer plane. The transducer acts both as a transmitter and, after some time delay, as a receiver. The piston surface area $A(x, y)$ is centered around point (x, y) .
- A planar scattering object is positioned in the reflector plane, which is parallel to the transducer plane at distance z_0 . The scattering object is described by its *object function*

$$f(x', y') = \begin{cases} 1 & \text{inside the scattering area } A' \\ 0 & \text{outside} \end{cases} \quad (2)$$

It is this object function f that we are interested in and which needs to be reconstructed from the received transducer signal $S(t, x, y)$. Let us assume that S is proportional to the force acting on the transducer surface¹

$$S(t, x, y) \sim \iint_{A(x, y)} dx'' dy'' p(t, x'', y'', z = 0) \quad (3)$$

¹Strictly speaking, the signal actually is a temporal convolution of the force with the transducer electro-mechanical transfer function [39]. Our assumption is equivalent to using a delta distribution as transfer function.

where $p(t, x, y, z)$ is the sound pressure field. For visualization, the time dependent signal $S(t, x, y)$ is usually converted to a grayscale image $S_C(x, y)$, also known as *C-scan*, hence the subscript *C*. For converting the time varying signal S at position (x, y) to a single gray value, different methods are possible. A commonly used approach is to use the maximum amplitude of the A-scan signal

$$S_C(x, y) = \max_{t_1 < t < t_2} |S(t, x, y)| \quad (4)$$

The pressure field $p(t, x, y, z)$ in Eq. (3) is subject to the wave equation

$$\nabla^2 p - \frac{1}{c^2} \frac{\partial^2 p}{\partial t^2} = 0 \quad (5)$$

where c is the sound velocity of the surrounding medium. Transducer and scattering object enter the mathematical formulation as boundary conditions whose type depend on the medium and the scattering material. In medical ultrasound, e.g., the scattering object is a density inhomogeneity in the medium, which requires a special theoretical model [18]. In our situation we consider two simpler special cases: scattering by a rigid object in a fluid medium, and scattering by a cavity in a solid medium.

2.1 Formal solution for the transducer force and the PSF

In the case of scattering at a cavity in a solid medium, we have a soft boundary where the pressure is zero at the cavity surface, thereby leading to a *Dirichlet boundary condition*. In the case of a hard boundary in a fluid medium, the particle velocity perpendicular to the boundary surface is zero. In the situation of Fig. 1, the boundary is perpendicular to the z -direction, so that the boundary condition prescribes the velocity in the z -direction $v_z(t, x, y)$. For a medium of density ρ , the relationship between pressure p and velocity \vec{v} is

$$\frac{\partial \vec{v}}{\partial t} = -\frac{1}{\rho} \nabla p \quad \Rightarrow \quad \frac{\partial v_z}{\partial t} = -\frac{1}{\rho} \frac{\partial p}{\partial z} \quad (6)$$

Hence the boundary condition at a hard scattering object is a condition upon the pressure gradient perpendicular to the boundary surface, which is a *von Neumann boundary condition*.

A solution of the wave equation does however not only require knowledge of the boundary conditions at the transducer and the diffraction object, but in the entire transducer and reflector planes. While closed form solutions, known as *Rayleigh integrals*, can be given for the sound field for pure Dirichlet or von Neumann boundary conditions, the same does not hold for mixed boundary conditions. Unfortunately, diffraction problems lead to mixed boundary conditions [19] and formal analytical solutions are only known for special cases like diffractions of plane waves by circular objects [20] [21] or point sources diffracted by an infinite half plane [22]. Approximate solutions for arbitrarily shaped reflection

objects can however be obtained with Kirchhoff's approximations or modifications thereof, as described by Bouwkamp [19].

As we show in the Appendix, within such an approximation the solution for the resulting transducer signal given by (3) can indeed be written in the form of a convolution between the object function $f(x, y)$ and a *point spread function* (PSF)

$$S(t, x, y) \sim -e^{i\omega t} \iint_{\mathbb{R}^2} dx' dy' f(x', y') g(x - x', y - y') \quad (7)$$

where the PSF $g(x, y)$ is given by

$$g(x, y) = \frac{i\omega\rho v_0}{4\pi^2} H(z_0, x, y) \left. \frac{\partial}{\partial z} H(z, x, y) \right|_{z=z_0} \quad (8)$$

where v_0 is the velocity amplitude of the transducer oscillating with frequency $\nu = \omega/2\pi$, ρ is the density of the medium, and H is given by

$$H(z, x, y) = \iint_{A(0,0)} d\xi d\eta \frac{e^{-ik\sqrt{z^2+(x+\xi)^2+(y+\eta)^2}}}{\sqrt{z^2+(x+\xi)^2+(y+\eta)^2}} \quad (9)$$

For point symmetric transducer surfaces $A(x, y) = A(-x, -y)$, the substitutions $x' = -\xi$ and $y' = -\eta$ lead to

$$H(z, x, y) = \iint_{A(0,0)} dx' dy' \frac{e^{-ik\sqrt{z^2+(x-x')^2+(y-y')^2}}}{\sqrt{z^2+(x-x')^2+(y-y')^2}} \quad (10)$$

which is exactly proportional to the Rayleigh integral that describes the pressure field generated by a baffled piston oscillating with constant frequency. As this problem has already been studied in the literature for some time, several approximation schemes for computing $H(z, x, y)$ are known [23] [24] [16] [25], some of which will be discussed in the next section.

2.2 Numerical computation of the PSF

It is in principle possible to compute the z -derivative in Eq. (8) analytically by drawing it under the integral. For a numerical evaluation, it is however more convenient not to do so because when we have a numerical routine for computing $H(z, x, y)$, we can also use it to compute its derivative numerically via

$$\left(H(z_0 + \Delta z) - H(z_0 - \Delta z) \right) / 2\Delta z \quad (11)$$

$$\text{or} \quad \left(H(z_0 + \Delta z) - H(z_0) \right) / \Delta z \quad (12)$$

Expression (11) has a smaller error of order Δz^2 , but requires three evaluations of H for computing the PSF in (8) (at z_0 , $z_0 - \Delta z$, and $z_0 + \Delta z$), while expression (12) requires only two evaluations of H , but has a larger error of order Δz .

A straightforward numerical method for evaluating $H(z, x, y)$ given by (10) is the *patch element method* (PEM) [16]. The idea is to decompose the transducer area

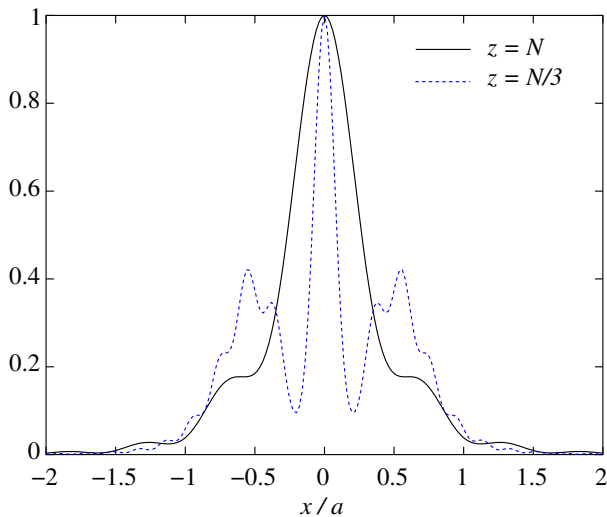


Fig. 2. Absolute value of the PSF perpendicular to the acoustical axis for two different values of the on axis distance z for a circular transducer area with radius $a = 5$ mm and $\lambda = 0.296$ mm. The PSF has been normalized to maximum value one. $N = (4a^2 - \lambda^2)/4\lambda \approx a^2/\lambda$ is the near field distance.

$A(0,0)$ into N rectangular patches of area $\Delta w \Delta h$ that are sufficiently small, so that the Fraunhofer approximation (see Sec. 2.3) holds for each patch. The resulting integrals can then be evaluated analytically and the integral over $A(0,0)$ is the sum of all patch contributions (compare Eq. (10) in [16])

$$H(z, x, y) \approx \Delta w \Delta h \sum_{n=1}^N \frac{e^{-ikR}}{R} \times \text{sinc} \frac{k(x-x_n)\Delta w}{2R} \cdot \text{sinc} \frac{k(y-y_n)\Delta h}{2R} \quad (13)$$

where (x_n, y_n) is the center of the n -th patch element, Δw and Δh are width and height of each patch element, and R^2 is $z^2 + (x-x_n)^2 + (y-y_n)^2$. The same idea was utilized by Rangarajan et al. to derive a numerical expression for the point spread function based on a heuristic model of the scattering process [7]. The patch element method can be used for arbitrary shapes A of the transducer surface.

For *circular* transducer surfaces $A(0,0)$, a transition to cylindrical coordinates allows for an analytic evaluation of one of the integrals in the double integral (10). Even though this results in different possible equivalent *single* integral expressions, like the Schoch integral [26], the King integral [27], or variants thereof [28] [29] [30], these are not necessarily better suited for a numerical evaluation. McGough et al. compared in [31] different equivalent integral expressions for (10), and found the smallest numerical error for Gaussian quadrature with

the following single line integral²:

$$H(z, x, y) = \frac{i2a}{k} \int_0^\pi d\varphi \frac{s \cos \varphi - a}{s^2 + a^2 - 2as \cos \varphi} \times \left(e^{-ik\sqrt{s^2+a^2-2as \cos \varphi+z^2}} - e^{-ikz} \right) \quad (14)$$

where $s^2 = x^2 + y^2$, and a is the radius of the transducer area.

Fig. 2 shows the absolute value of the PSF computed with equations (14), (11), and (8), where the integral in (14) has been evaluated with the GNU OCTAVE function *quadgk*³. The shape of the PSF is identical to Fig. 2b in [7], as should be expected because Huygen's principle, on which the numerical method by Rangarajan et al. is based, is a reformulation of the first Rayleigh integral and therefore also makes the approximation of the modified Kirchhoff theory. In other words, our solution (8) is the exact analytical expression for which Rangarajan et al. have given one particular numerical approximation scheme in [7].

2.3 Analytical computation of the PSF

For two special cases of a circular piston with radius a , we can derive closed analytic expressions for the PSF: on the acoustical axis and in the far-field approximation. These solutions are not only useful as a ground truth against which the numerical solutions can be compared, but they provide also insight into the qualitative behavior of the PSF.

On the *acoustical axis*, we have $x = y = 0$ so that the integral (10) can be directly evaluated in cylindrical

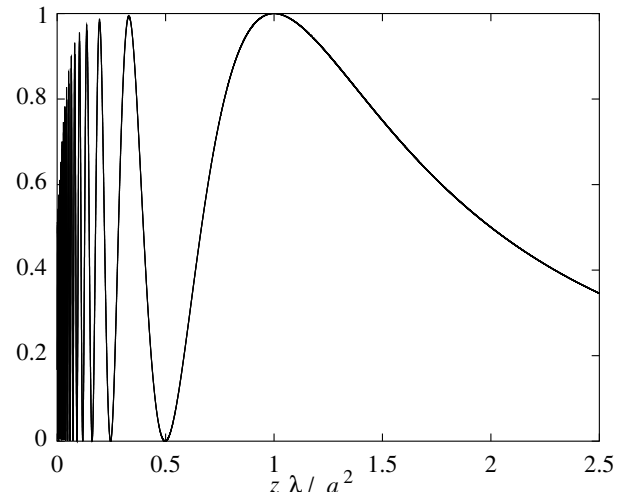


Fig. 3. Absolute value of the PSF for a circular transducer area with radius $a = 5$ mm along the acoustical axis (i.e. $x = y = 0$) for $\lambda = 0.296$ mm. The curve has been normalized to maximum value one.

²Note that the term called H by McGough et al. [31] corresponds to $-H/2\pi$ in our notation.

³See <http://www.octave.org/>

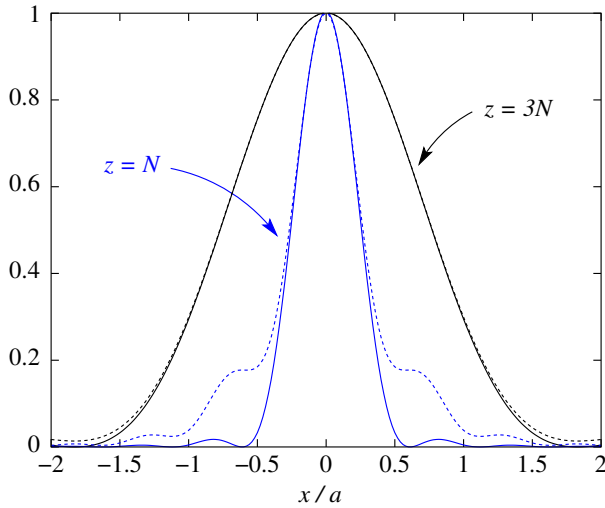


Fig. 4. Comparison of the far-field approximation (solid) for the absolute value of the PSF with the numerical solution (dotted) for a circular transducer area with radius $a = 5$ mm and $\lambda = 0.296$ mm.

coordinates to

$$H(z, 0, 0) = \int_0^{2\pi} d\varphi \int_0^a dr r \frac{e^{-ik\sqrt{z^2+r^2}}}{\sqrt{z^2+r^2}} \quad (15)$$

$$= \frac{i4\pi}{k} e^{-ik(z+\sqrt{z^2+a^2})/2} \sin \frac{k(z-\sqrt{z^2+a^2})}{2}$$

The resulting amplitude $|g|$ of the PSF given by (8) is then proportional to $|H\partial_z H|$ and is shown in Fig. 3.

In the *far-field approximation* $z \gg a$, which is in optics also known as the Fraunhofer approximation, the term R in the integral (10) is replaced by $R \approx r = \sqrt{x^2 + y^2 + z^2}$ in the denominator and by $R \approx r - (xx' + yy')/r$ in the exponent:

$$H(z, x, y) \stackrel{z \gg a}{\approx} \frac{e^{-ikr}}{r} \iint_{A(0,0)} dx' dy' e^{ik(xx' + yy')/r} \quad (16)$$

For a circular piston with radius a , this integral can be evaluated analytically to [23]

$$H(z, x, y) \approx \frac{e^{-ikr}}{r} \frac{2\pi a^2}{ka \sin \theta} J_1(ka \sin \theta) \quad (17)$$

where $r = \sqrt{x^2 + y^2 + z^2}$, and $\sin \theta = \sqrt{x^2 + y^2}/r$, and J_1 is the Bessel function of the first kind and first order [32]. Fig. 4 compares the resulting far-field PSF amplitude $|g| \sim |H\partial_z H|$ with the numerical solution based on (14) for different values of the on-axis distance z .

3 DECONVOLUTION SCHEMES

In section 2, we have derived an expression for the C-scan image (4) from the wave equation which is based on fundamental physical principles. This is however not the only way in which the imaging process can be modeled. In *linear system theory* (LST), the imaging process is

modeled as a black box operation that transforms the object function f into a C-scan image $S_C[f]$. Under the assumption that this mapping is linear and position-invariant, the most general form of this mapping is [8]

$$S_C[f] = f * h \quad (18)$$

where the symbol “*” denotes a two dimensional convolution

$$(f * h)(x, y) = \iint_{\mathbb{R}^2} dx' dy' f(x', y') h(x - x', y - y')$$

and $h(x, y)$ is an unknown point spread function (PSF) that completely describes the imaging system. The term “point spread function” stems from the fact that it is the image of a point scatterer located in the origin, as can be seen by inserting $f(x', y') = \delta(x', y')$ into (18).

To see how linear system theory relates to the imaging model from section 2, we can insert $f = \delta$ into equations (7) and (4). It follows that the PSF from linear system theory is given by $|g(x, y)|$, where g is given by equation (8). It should be noted however, that in general equation (18) does not hold, because the C-scan image according to (4) and (7) is given by $|f * g|$, which in general is not identical to $f * |g|$ because, even though f is real and non-negative, g in general is not real and positive. In other words, the physical model of section 2 can only be reformulated in terms of linear system theory under the assumption that

$$|f * g| \approx f * |g| \quad \text{for all } x, y \quad (19)$$

Let us call this assumption the *LST approximation*. Although it looks like a crude approximation, the experimental results in section 4 show that this approximation actually works quite well.

In the framework of linear system theory, the problem of reconstructing the object function f from an image S_C is known as the *deconvolution problem*. Whereas the PSF h is known in our situation, there is still an unknown term because an actual pulse-echo image is always disturbed by some noise $\eta(x, y)$:

$$S_C = f * h + \eta \quad (20)$$

For approximately solving this equation for f , there are different algorithms, three of which we discuss in the following subsections.

3.1 Wiener filter

The *Wiener filter* is the most popular deconvolution algorithm because it can be expressed as a closed analytic formula for estimating the object function f [8]:

$$f \approx \mathcal{F}^{-1} \left(\frac{\mathcal{F}(S_C)}{\mathcal{F}(h)} \cdot \frac{|\mathcal{F}(h)|^2}{|\mathcal{F}(h)|^2 + K} \right) \quad (21)$$

where \mathcal{F} denotes the two-dimensional Fourier transform and \mathcal{F}^{-1} its inverse, and K is a regularization constant acting as a free parameter for optimizing the result. It

should be noted that (21) is not guaranteed to be real and positive, so that the real part of (21) needs to be taken and negative values must be set to zero.

The Wiener filter has been shown to improve degraded images both in x-ray radiography [9] and in ultrasonic imaging [7]. It has however the disadvantage of creating ringing artifacts at edges and performed poorer than other deconvolution methods in the comparative study by Verbeeck and Bertoni [14].

3.2 Richardson-Lucy algorithm

The *Richardson-Lucy algorithm*, also known as the *expectation maximization* method, is an iterative scheme that computes successive improved images f_n from the starting point $f_0 = S_C$ [33]:

$$f_{n+1} = \left(\frac{S_C}{h * f_n} * \bar{h} \right) \cdot f_n \quad (22)$$

where $\bar{h}(x, y) = h(-x, -y)$, which is the same as $h(x, y)$ for symmetric point spread functions h . The Richardson-Lucy algorithm is commonly deployed in astronomy [34] and microscopy [35]. In the comparative study [14], it performed better than the Wiener filter.

A problem with the iteration (22) is that it amplifies noise so that for $n \rightarrow \infty$ the image consists of noise only. This makes it tricky to apply because the iteration needs to be stopped before too much noise is amplified. Therefore different regularization schemes have been proposed to achieve actual convergence of the iteration, like the total variation regularization by Dey et al. [15]:

$$f_{n+1} = \left(\frac{S_C}{h * f_n} * \bar{h} \right) \cdot \frac{f_n}{1 - \lambda \operatorname{div} \left(\frac{\operatorname{grad} f_n}{|\operatorname{grad} f_n|} \right)} \quad (23)$$

where div is the divergence, and grad is the gradient, where the partial derivatives can be computed, e.g., with Eq. (11) with a step width of one pixel. It should be noted that this regularization can lead to a division by zero or even to a negative f_n in some cases, so that the regularization parameter λ must not be too large. Dey et al. recommended $\lambda = 0.002$ and used the convergence criterion

$$\frac{\sum_x \sum_y |f_{n+1}(x, y) - f_n(x, y)|}{\sum_x \sum_y f_n(x, y)} < \text{some threshold} \quad (24)$$

3.3 ForWaRD

The problem that the Wiener filter introduces artifacts at edges is specifically addressed by the *ForWaRD* deconvolution scheme by Neelamani et al. [10]. To this end, they have reformulated the traditional Wiener filter based on the Fourier transform (21) as a “shrinkage” operation on the Fourier expansion of the object function. This formulation can be generalized to other expansions like the wavelet transform, thereby leading to a *wavelet Wiener filter* (WWF). In the *ForWaRD* deconvolution, the Wiener filter is followed by a WWF, which acts as a nonlinear denoising operation.

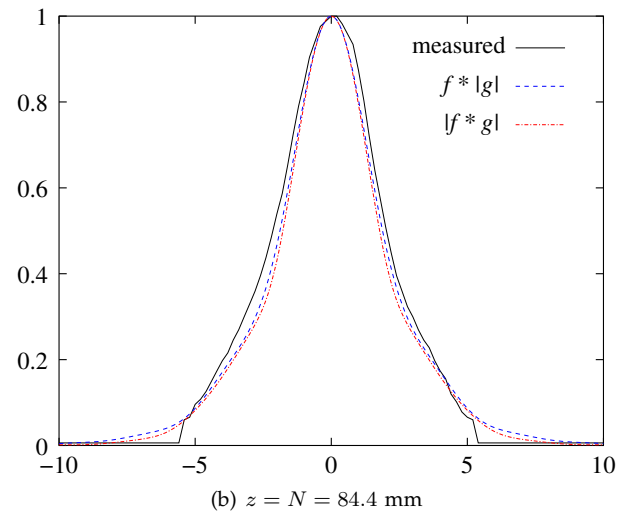
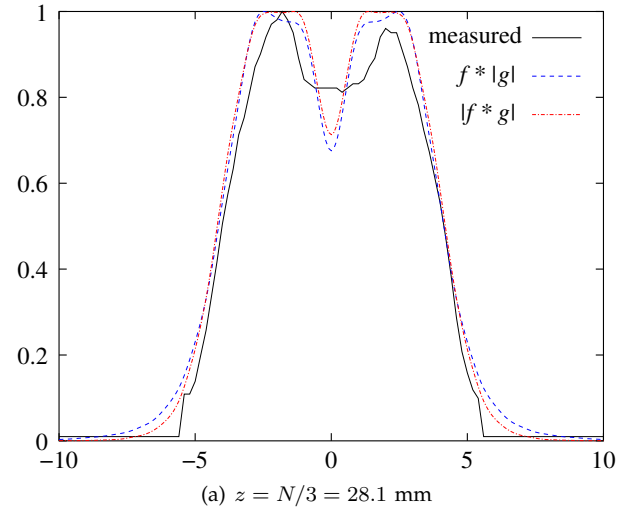


Fig. 5. Comparison of the measured C-scan signal along the x -direction for a circular disk f with radius 1.5 mm with the convolutions $f * |g|$ and $|f * g|$.

Details of the algorithm and its parameter determination can be found in [10], or [11]. Moreover, Neelamani has made a demo application available which includes source code of an implementation of this algorithm⁴. In the study [11], the *ForWaRD* algorithm was applied to x-ray phase contrast images and showed better results than the Wiener filter.

4 EXPERIMENTS AND RESULTS

All measurements have been made with a circular H5K transducer (GE Sensing & Inspection Technologies GmbH, Robert-Bosch-Straße 3, 50354 Hürth, Germany). The radius was $a = 5$ mm and the mean frequency $\nu = 5$ MHz which corresponds to a wavelength $\lambda = 0.296$ mm in the medium water. The relative bandwidth (-6 dB) of this transducer was ± 2.5 MHz, so that replacing the frequency spectrum with a single mean frequency might look like a crude approximation at first sight. The

⁴<http://dsp.rice.edu/software/forward>

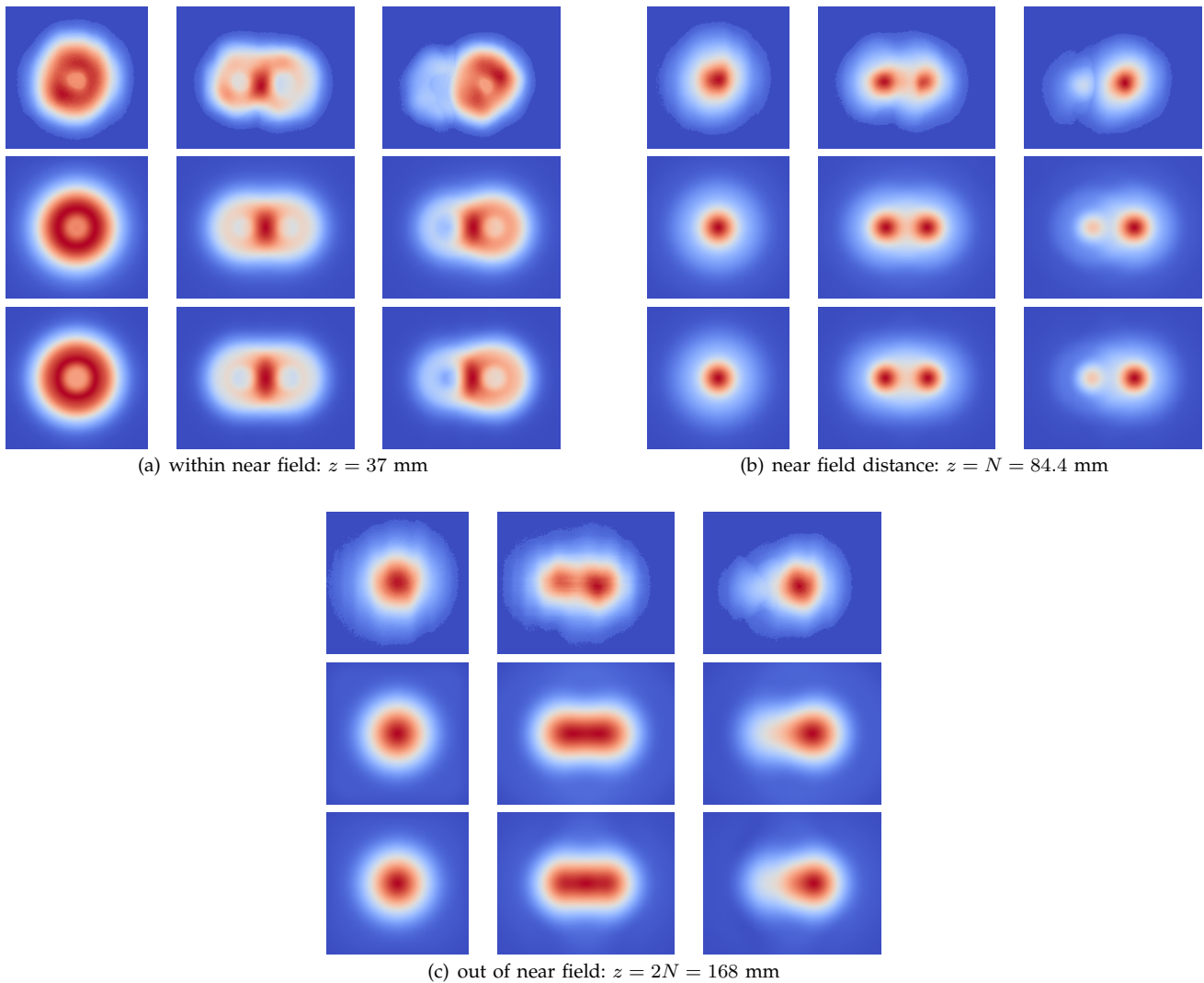


Fig. 6. Comparison of the measured C-scan image (top row) with the convolutions $f * |g|$ (middle row) and $|f * g|$ (bottom row) for three different objects f : a single disc (left column), two disks of identical size (middle column), and two disks of different size (right column). All images are 16 mm high, the narrower images are 16 mm wide, and the wider images are 20 mm wide.

experimental results in this section demonstrate however that this approximation actually works quite well, both for simulating the C-scan image and for deconvolution.

With this system, we have recorded C-scan images of the (x, y) -plane with a resolution of 0.1 mm at different on-axis distances z for the following three scattering objects:

- a circular disk of radius 1.5 mm
- two circular disks of radius 3 mm with center distance 5 mm
- two circular disks with radii 2 mm and 3 mm with center distance 5 mm

We have used these images in two ways:

- 1) to compare them with a simulated image obtained from a convolution between object function and PSF
- 2) to deconvolve them and compare the result with the known object function

The first point allows to evaluate how well our PSF

and the LST approximation describe the C-scan imaging process, and the second point allows for a comparison of the different deconvolution algorithms.

4.1 Validation of the LST approximation

To evaluate the validity of the LST approximation and of our physical model, we have simulated C-scan images by means of both sides of equation (19) with the PSF given by equations (8), (14), and (11) for different objects f and for different on axis distances z . All convolutions have been computed with the OCTAVE function `conv2`, which directly computes the convolution. This is slower than an FFT based convolution, but does not introduce an imaginary part and is more accurate.

Fig. 5 shows the signal intensity distribution for a circular disk. Due to the rotational symmetry of this geometry, all information is visible along the x -direction for $y = 0$. The two on-axis distances z are the same as for the PSFs shown in Fig. 2. As can be seen, the model

describes the shape of the signal intensity quite well. In Fig. 5(a), the difference between $f * |g|$ and $|f * g|$ is smaller than the difference to the measured signal. We conclude that the LST approximation works quite well in our situation and introduces a smaller error than other assumptions in our model, namely the assumption of a single frequency ω of the transducer.

The same conclusion can be drawn from the two-dimensional C-scan images in Fig 6, which have been colorized in the online version of this article with a *diverging colormap* after Moreland [36], as implemented in the function `false_color` of the Python library GAMERA⁵: red represents high values, blue represents low values, and light gray represents medium values. Differences between $f * |g|$ and $|f * g|$ are barely noticeable, and the shape of the signal intensity in the measured signal corresponds to the shape in the simulated images.

4.2 Evaluation of deconvolution schemes

We have implemented the Wiener filter and the Richardson-Lucy algorithm in GNU OCTAVE, and the ForWaRD algorithm in C++ based on the code by Neelamani. To find a good choice for the parameter K in the Wiener filter, we have computed the mean square error between the deconvolution of known convolutions $f * |g|$ and the object function f , because the Wiener filter tries to minimize this error [8]. Depending on the on-axis distance z and the object function f , the minimum error occurred for values K between 100 and 1000, so that we have settled on $K = 500$. For the Richardson-Lucy (RL) algorithm, we have set the number of iterations to 30, and for the total variation regularization (RL-TV), we have set the convergence threshold to 0.5%, because for smaller values we had not observed a satisfying convergence.

We had thus four different deconvolution algorithms which we have compared both on simulated and real pulse-echo images. The PSFs for simulation and deconvolution have been numerically computed with Eqs. (8), (11), and (14). Moreover, we have tested how well the far-field approximation (17) of the PSF works even when the on-axis distance is not yet in the far-field region.

4.2.1 Simulated images

As all deconvolution algorithms make the assumption that the image is of the form $f * |g|$ where f is the object and $|g|$ is the PSF, we have tested first how the algorithms compare when this assumption exactly holds. To this end, we have applied the algorithms to the images in the second rows of Fig. 6. Note that in these images, no noise was artificially added. In other words the only noise was due to numerical inaccuracies and to digitization errors from the 0.1 mm rastering.

Fig. 7 shows the deconvolution results along the $y = 0$ axis for two disks of different size. This is the most

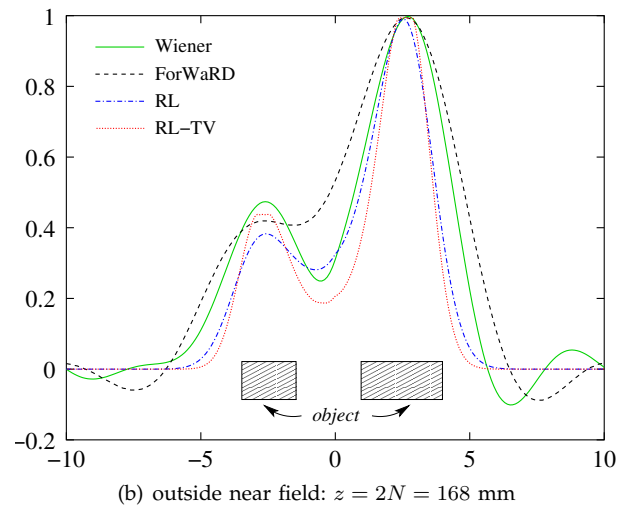
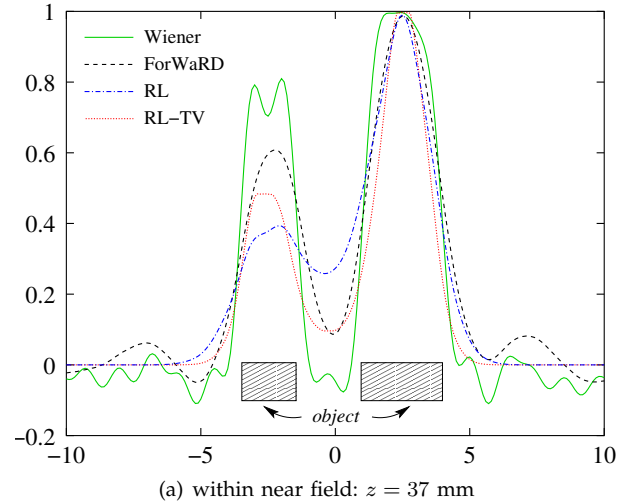


Fig. 7. x -axis cuts at $y = 0$ of the different deconvolution results for simulated images of two circular discs with radii 1 mm and 1.5 mm.

difficult of our three object configurations because the echo of the smaller disk is weaker and tends to be swallowed by the echo of the larger disk. With the exception of the ForWaRD algorithm for $z = 2N$, all algorithms can separate the two echoes. The Wiener filter creates the strongest contrast in the near field, while outside the near field the regularized Richardson-Lucy algorithm results in a slightly stronger contrast. The Wiener filter and the ForWaRD algorithm however introduce oscillations with negative values, which are particularly strong for the Wiener filter in the near field. Even when these are truncated, the positive local maxima from these oscillations remain and introduce artifacts into the deconvolved image. The ForWaRD algorithm smoothes the oscillations, but this has the side effect that the echoes are poorly separated in the far field. The Richardson-Lucy algorithm, especially in its regularized form with an automatic selection of the number of iterations, shows the best result in all cases: the deconvolved images only have two local maxima which are clearly separated.

For the simulated images, we have also tested the ro-

⁵See <http://gamera.sf.net/>

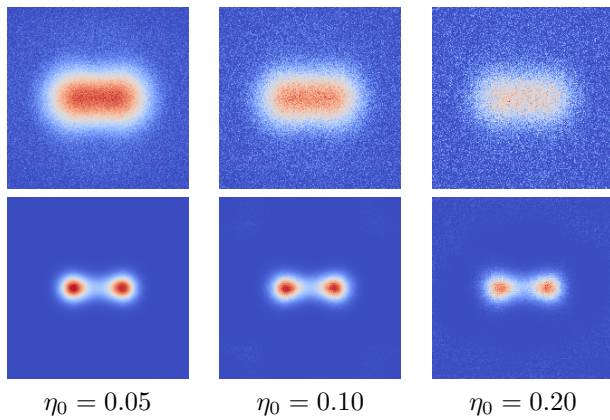


Fig. 8. Results (bottom) of the Richardson-Lucy algorithm with total variation regularization at different noise levels $\eta_0 = \sigma / \max(f * |g|)$ for simulated images (top) with additive Gaussian noise with variance σ^2 .

bustness of the Richardson-Lucy algorithm with respect to noise. To this end, we have added Gaussian noise η with variance σ^2 to the result of the convolution:

$$S_C = \max\{f * |g| + \eta, 0\} \quad (25)$$

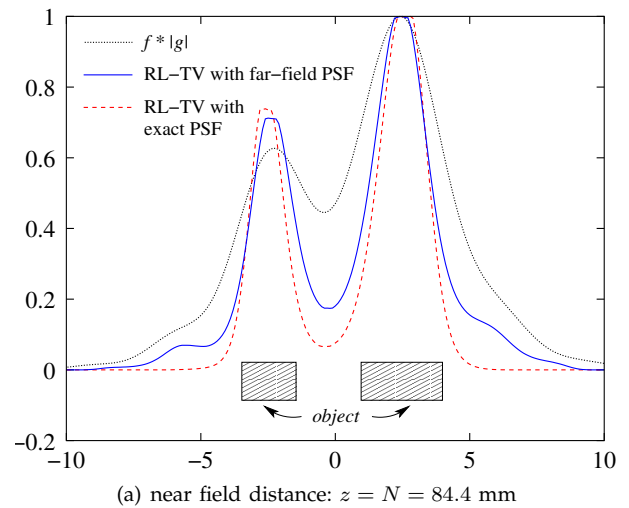
where the maximum has been applied to avoid negative signal intensities in the simulated image. As can be seen in Fig. 8, even for high noise levels, the total variation regularization of the Richardson-Lucy algorithm is very robust with respect to noise. This is in agreement with the results by Dey et al. [15].

4.2.2 Real images

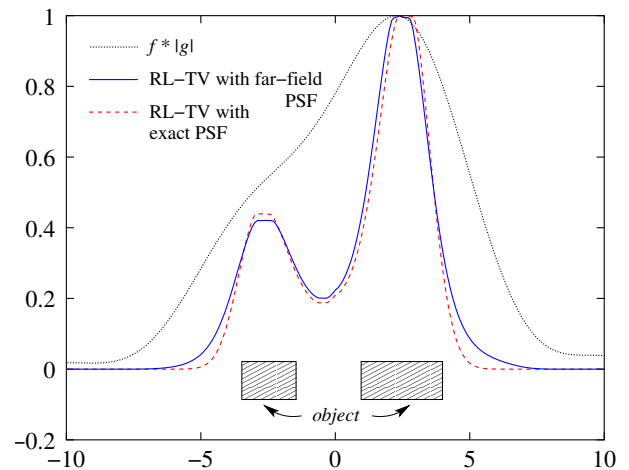
On the real images, similar effects can be observed for the deconvolution results shown in Fig. 9. The Wiener filter works best at the near field distance, for which it actually produces a sharper minimum between the two disks than the other algorithms, at the expense of slight oscillations near to the objects. In the near and far field however, these oscillations create serious artifacts: in the near field the larger disk of the object in the bottom row appears to be split up into more than one component, and in the far field the smaller disk in the bottom row is indistinguishable from the artifacts created by the Wiener filter.

The ForWARD algorithm produces weaker artifacts at the expense of a less clear separation of echoes. Like the Wiener filter, the ForWARD algorithm works best at the near field distance N . In the near field, it introduces stronger artifacts than in the far field, but the echoes are considerably poorer separated in the far field: the spread of the echoes at large distances is larger than for the Wiener filter.

The Richardson-Lucy algorithm performs best in all cases: It introduces no artifacts at all and results in exactly the number of local maxima as there are real objects. Like the other algorithms, the echoes remain wider spread in the far field, but, unlike the other algorithms, it performs even better in the near field than at the near



(a) near field distance: $z = N = 84.4$ mm



(b) outside near field: $z = 2N = 168$ mm

Fig. 10. x -axis cuts at $y = 0$ of the RL-TV deconvolution for simulated images of two circular discs with radii 1 mm and 1.5 mm, which are represented by an object function f according to (2). In the solid curves, the PSF g was replaced by its far field approximation in the deconvolution, while the dotted curve was obtained with the numerically computed exact PSF.

field distance N . This is particularly impressive because the original image has *minima* at the object locations due to interference effects, which are perfectly restored as *maxima*.

4.2.3 Far field approximation

The far field approximation (17) avoids the numerical integration in the computation of the PSF and can thus be desirable to use in practice. It is therefore interesting to see how well it works even outside the actual far field region. As the far field approximation always has its maximum value on the acoustical axis $x = y = 0$, we cannot expect it to work in the near field, where the PSF can even have a local minimum at $x = y = 0$ (see Fig. 3). Hence, it only makes sense to try the far field approximation for $z > N \approx a^2/\lambda$.

Fig. 10 shows the result of the best performing deconvolution algorithm (RL-TV) on simulated images $f * |g|$

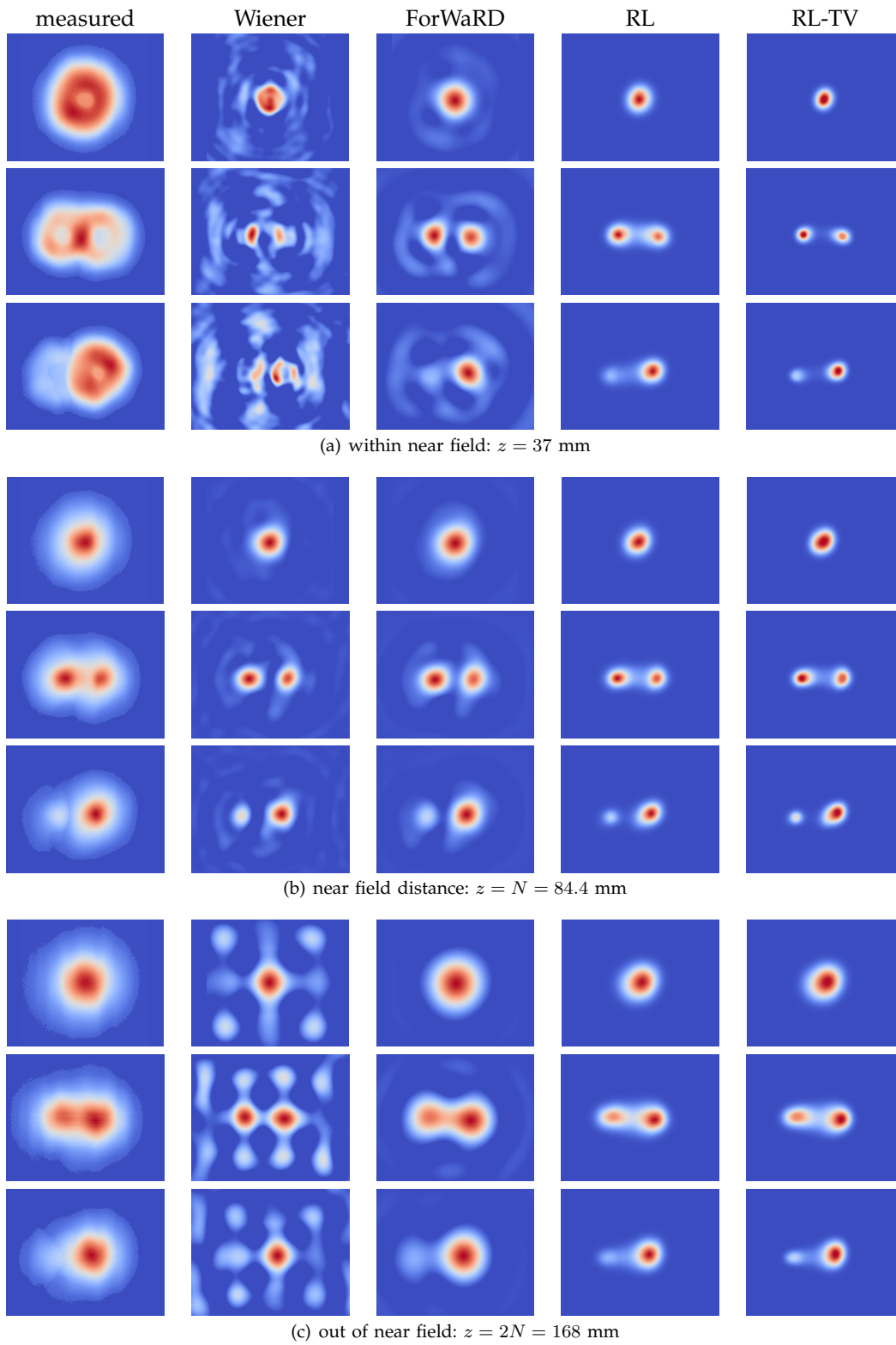


Fig. 9. Results of the different deconvolution algorithms on real pulse-echo images (left column): RL stands for the Richardson-Lucy algorithm with 30 iterations, and RL-TV for the Richardson-Lucy algorithm with total variation regularization. Negative values in the results of the Wiener and ForWaRD filters have been truncated to zero. All images are 20 mm wide and 16 mm high.

when the PSF $|g|$ in the deconvolution is replaced by its far field approximation. For $z = 2N$ the approximation works quite well, while it works poorer for $z = N$, as was to be expected. Even for $z = N$ however, a deconvolution with the far field approximated PSF improves the image.

4.2.4 Runtime considerations

All computations have been done without parallelization with GNU OCTAVE 3.2.4 on an Intel i7-4770 CPU 3.40GHz. The computation of a 200×200 PSF took 10 sec with Eqs. (14) and (11), and 7 sec with Eqs. (14) and (12), due to about one third fewer evaluations of H . The computation of the far-field PSF with Eqs. (17) and (11) took only 0.5 sec. Although the far-field approximation saves considerable runtime, it should be noted that the PSF needs to be computed only once for a given on-axis distance z . It can therefore be tabulated beforehand and has little impact on the total runtime of the deconvolution under production conditions.

The Richardson-Lucy deconvolution with total variation regularization took about 3 min for a 200×200 image with the OCTAVE function `conv2`, but only 3 sec with taking instead the real part of `fftconv2` (a convolution implementation by means of a fast Fourier transform). It should be noted that the processing time presumably can be further reduced significantly by utilizing speedup techniques for the Richardson-Lucy algorithm like those described in [37] [38].

In any case, even when the PSF is computed on the fly, the deconvolution can be done in real-time, because the runtime for the convolution is less than the run-time for capturing the C-scan pulse-echo image.

5 CONCLUSION

We have presented an analytical expression for the PSF of ultrasonic pulse-echo imaging that was in good agreement with our experiments. It can be used for non-blind deconvolution by computing the PSF numerically or (for $z \geq 2a^2/\lambda$) analytically. As a deconvolution scheme, we would recommend the Richardson-Lucy algorithm because it showed the best results in our experiments. With the total variation regularization, the convergence of the Richardson-Lucy algorithm occurred typically between 50 and 100 iterations, so that, as an alternative to the regularization, the original Richardson-Lucy algorithm might be applied with 50 iterations to ultrasonic images as a rule of thumb, but even with fewer iterations the results are satisfying.

In our derived formula for the PSF, we have made the assumption of a single frequency of the transducer. Although this was only a crude approximation for our experiments, the results were nevertheless quite good. It would be interesting to investigate whether the agreement between experiment and theory can be further improved by taking the exact shape of the transducer frequency spectrum into account.

The PSF presented in this article only holds for sound propagation through a single isotropic medium. This means that our solution cannot be applied directly to ultrasonic inspection of solid media. Even though we show in the appendix that the PSFs for hard scatterers (obstacles in fluids) and soft scatters (holes in solids) are identical, the assumption of a single medium does not hold for the ultrasonic inspection of solid materials, because the latter typically are coupled with the transducer through another fluid medium. In the case of a planar medium transition, both media might be approximated through a single medium with an *effective path* concept [7]. This conjecture however requires a closer experimental and theoretical investigation.

Another interesting point is that our experiments have shown a surprisingly good agreement between $f*|g|$ and $|f*g|$ (the LST approximation). As it is not clear which special properties of f and g justify this approximation in our case, another interesting subject for future research would be to determine under which circumstances this approximation holds from a mathematical approximation theory point of view.

APPENDIX A

ANALYTICAL EXPRESSION FOR THE SOUND FIELD OF HARD SCATTERERS

While the boundary condition at the transducer only depends on the known transducer velocity $v_z(t, x, y)$, the boundary condition at the scattering object depends on its material. When the scatterer is a rigid object, it is $v_z = 0$ at its surface. Moreover, we assume the transducer velocity to be the same over its entire area, i.e. $v_z(t, x, y) = v_z(t)$, which leads to the following boundary conditions

$$\frac{\partial p}{\partial z} = \begin{cases} -\rho \dot{v}_z(t) & \text{at the transducer} \\ 0 & \text{at the scatterer} \end{cases} \quad (26)$$

where the dot denotes a time derivative. To solve the wave equation, it is convenient to decompose the total pressure field p into a sent pressure field p_{sent} and a scattered pressure field p_{scat}

$$p(t, \vec{x}) = p_{sent}(t, \vec{x}) + p_{scat}(t, \vec{x}) \quad (27)$$

When the transducer is in sender mode, p_{scat} is zero near the transducer surface, and when it is in receiver mode, p_{sent} is zero near the transducer surface. The received transducer signal is therefore p_{scat} alone, so that this pressure field is the interesting observable.

For completely determining the pressure field, the boundary condition (26) needs to be extended into the entire transducer and scatterer plane. To avoid the problem of mixed boundary conditions, an often made approximation is that of the modified Kirchhoff theory (see [19], section 4):

$$\frac{\partial p_{sent}}{\partial z} = \begin{cases} -\rho \dot{v}_z(t) & \text{inside the transducer area } A(x, y) \\ 0 & \text{elsewhere in the transducer plane} \end{cases} \quad (28)$$

When the transducer is mounted on a rigid wall (a baffled transducer), this boundary condition holds exactly, but for most practical situations it is merely an approximation. The solution of the wave equation (5) under this boundary condition is given by the Rayleigh integral⁶ [23] (for other, equivalent expressions see [24])

$$p_{sent}(t, x, y, z) = \frac{\rho}{2\pi} \iint_A dx' dy' \frac{\dot{v}_z(t - R/c)}{R} \quad (29)$$

where A is the transducer surface area and R^2 is $z^2 + (x - x')^2 + (y - y')^2$. For the constant frequency case $v_z(t) = v_0 e^{i\omega t}$, where $\omega = 2\pi c/\lambda = ck$ (c denotes the velocity of sound, λ the wavelength, and k the wavenumber), this becomes

$$p_{sent}(t, x, y, z) = \frac{i\omega\rho v_0}{2\pi} e^{i\omega t} \iint_A dx' dy' \frac{e^{-ikR}}{R} \quad (30)$$

Inside the scattering area, the hard boundary condition (26) leads to

$$\frac{\partial p}{\partial z} = 0 \quad \Rightarrow \quad \frac{\partial}{\partial z} p_{scat} = -\frac{\partial}{\partial z} p_{sent}$$

Outside the scattering area A' and $z \geq z_0$, we make the modified Kirchhoff approximation again and obtain as boundary conditions for the scattered field at $z = z_0$

$$\frac{\partial p_{scat}}{\partial z} = \begin{cases} -\frac{\partial}{\partial z} p_{sent} & \text{inside the scattering area } A' \\ 0 & \text{elsewhere in the scatterer plane} \end{cases} \quad (31)$$

This boundary condition is formally identical to (28), and the solution is again given by the Rayleigh integral

$$p_{scat}(t, x, y, z_0 - z) = -\frac{1}{2\pi} \iint_{A'} dx' dy' \frac{\frac{\partial}{\partial z} p_{sent}(t - R/c, x', y', z = z_0)}{R} \quad (32)$$

Inserting (32) and (30) into (3), we obtain for the received signal

$$\begin{aligned} S(t, x, y) &\sim \iint_{A(x,y)} dx''' dy''' p_{scat}(t, x''', y''', z = 0) \\ &= -e^{i\omega t} \iint_{A(x,y)} dx''' dy''' \iint_{A'} dx' dy' \frac{i\omega\rho v_0 e^{-ikR_0'''}}{4\pi^2 R_0'''} \times \\ &\quad \iint_{A(x,y)} dx'' dy'' \frac{\partial}{\partial z} \left(\frac{e^{-ikR''}}{R''} \right) \Big|_{z=z_0} \end{aligned} \quad (33)$$

where $R_0''^2 = z_0^2 + (x''' - x')^2 + (y''' - y')^2$ and $R''^2 = z^2 + (x'' - x')^2 + (y'' - y')^2$. After expressing the integral over A' with the object function (2) by writing

$$\iint_{A'} dx' dy' \dots = \int_{-\infty}^{\infty} \int_{-\infty}^{\infty} dx' dy' f(x', y') \dots \quad (34)$$

⁶Actually this is the *first* Rayleigh integral, but in most of the literature this is simply called *the* Rayleigh integral.

and after exchanging of the first two integrals and substituting $x''' = \xi + x$, $y''' = \eta + y$, and $x'' = \xi' + x$, $y'' = \eta' + y$, equation (33) becomes

$$S(t, x, y) \sim -e^{i\omega t} \int_{-\infty}^{\infty} \int_{-\infty}^{\infty} dx' dy' f(x', y') g(x - x', y - y') \quad (35)$$

where $g(x, y)$ is given by

$$g(x, y) = \frac{i\omega\rho v_0}{4\pi^2} H(z_0, x, y) \frac{\partial}{\partial z} H(z, x, y) \Big|_{z=z_0} \quad (36)$$

with

$$H(z, x, y) = \iint_{A(0,0)} d\xi d\eta \frac{e^{-ik\sqrt{z^2 + (x+\xi)^2 + (y+\eta)^2}}}{\sqrt{z^2 + (x+\xi)^2 + (y+\eta)^2}} \quad (37)$$

Eq. (35) shows that the received time dependent signal can be written as a spatial convolution of the object function with a *point spread function* (PSF) g .

APPENDIX B ANALYTICAL EXPRESSION FOR THE SOUND FIELD OF SOFT SCATTERERS

When the scattering object is a cavity, the boundary condition at the the scatterer does not impose a vanishing velocity, but vanishing pressure, i.e. $p(z_0) = 0$ inside the scattering area A' . With the decomposition (27) of the sound field into a sent and scattered field, this condition becomes

$$p = 0 \quad \Rightarrow \quad p_{scat} = -p_{sent}$$

To extend this boundary condition beyond the scattering area, the modified Kirchhoff theory suggests to simply set the scattered pressure to zero in the scattering plane outside the scattering area [19]:

$$p_{scat} = \begin{cases} -p_{sent} & \text{inside the scattering area } A' \\ 0 & \text{elsewhere in the scatterer plane} \end{cases} \quad (38)$$

The solution for this boundary condition is given by the *second* Rayleigh integral [20]

$$p_{scat}(t, x, y, z_0 - z) = -\frac{1}{2\pi} \iint_{A'} dx' dy' \frac{\partial}{\partial z} \frac{p_{sent}(t - R/c, x', y', z = z_0)}{R} \quad (39)$$

where R^2 is $z^2 + (x - x')^2 + (y - y')^2$. The sent field p_{sent} is the same as for a hard scatterer, and is thus given by (29). Inserting (29) into (39), we obtain for the received

signal

$$\begin{aligned}
 S(t, x, y) &\sim \iint_{A(x,y)} dx'' dy'' p_{scat}(t, x'', y'', z=0) \\
 &= -e^{i\omega t} \iint_{A(x,y)} dx'' dy'' \iint_{A'} dx' dy' \frac{i\omega \rho v_0}{4\pi^2} \times \\
 &\quad \frac{\partial}{\partial z} \left(\frac{e^{-ikR''}}{R''} \right) \Bigg|_{z=z_0} \iint_{A(x,y)} dx'' dy'' \frac{e^{-ikR_0''}}{R_0''} \quad (40)
 \end{aligned}$$

where $R_0''^2 = z_0^2 + (x''' - x')^2 + (y''' - y')^2$ and $R''^2 = z^2 + (x'' - x')^2 + (y'' - y')^2$. Again, we express the integral over A' with the object function f , make the substitutions $x''' = \xi + x$, $y''' = \eta + y$, and $x'' = \xi' + x$, $y'' = \eta' + y$, and obtain

$$S(t, x, y) \sim e^{i\omega t} \int_{-\infty}^{\infty} \int_{-\infty}^{\infty} dx' dy' f(x', y') g(x - x', y - y') \quad (41)$$

where $g(t, x, y)$ is given by

$$g(x, y) = -\frac{i\omega \rho v_0}{4\pi^2} \frac{\partial}{\partial z} H(z, x, y) \Bigg|_{z=z_0} H(z_0, x, y) \quad (42)$$

with

$$H(z, x, y) = \iint_{A(0,0)} d\xi d\eta \frac{e^{-ik\sqrt{z^2+(x+\xi)^2+(y+\eta)^2}}}{\sqrt{z^2+(x+\xi)^2+(y+\eta)^2}} \quad (43)$$

Within the modified Kirchhoff approximation, we thus obtain the same expression for the transducer signal both for soft and hard scatterers.

ACKNOWLEDGMENT

The authors thank Relesh Neelamani for making sample code of his implementation of the ForWaRD algorithm available, and Knut Verhoeven, Daniel Esser, and Imad El Mouakibi for porting this code to a C++ function. All other algorithm implementations and the numerical data analysis have been done with the free software package GNU OCTAVE. We also thank the anonymous reviewers for their valuable comments.

REFERENCES

- [1] D. Kundur and D. Hatzinakos, "Blind image deconvolution," *Signal Processing Magazine, IEEE*, vol. 13, pp. 43–64, May 1996.
- [2] C. Yu, C. Zhang, and L. Xie, "A blind deconvolution approach to ultrasound imaging," *Ultrasonics, Ferroelectrics, and Frequency Control, IEEE Transactions on*, vol. 59, pp. 271–280, February 2012.
- [3] L.-T. Chira, J.-M. Girault, and C. Rusu, "Into the ultrasound deconvolution using clean algorithm - statistical analysis of scatters detection," in *Electronics and Telecommunications (ISETC), 2012 10th International Symposium on*, 2012, pp. 299–302.
- [4] N. Rao, S. Mehra, J. Bridges, and S. Venkatraman, "Experimental point spread function of FM pulse imaging scheme," *Ultrasonic imaging*, vol. 17, pp. 114–141, 1995.
- [5] M. Sapia, M. Fox, L. Loew, and J. Schaff, "Ultrasound image deconvolution using adaptive inverse filtering," in *Computer-Based Medical Systems, 1999. Proceedings. 12th IEEE Symposium on*, 1999, pp. 248–253.

- [6] M. Alessandrini, L. De Marchi, and N. Speciale, "Recursive least squares adaptive filters for ultrasonic signal deconvolution," in *Circuits and Systems, 2008. ISCAS 2008. IEEE International Symposium on*, 2008, pp. 2937–2940.
- [7] R. Rangarajan, C. Krishnamurthy, and K. Balasubramaniam, "Ultrasonic imaging using a computed point spread function," *IEEE Transactions on Ultrasonics, Ferroelectrics, and Frequency Control*, vol. 55, pp. 451–464, 2008.
- [8] R. Gonzalez and R. Woods, *Digital Image Processing*, 2nd ed. New Jersey: Prentice-Hall, 2002.
- [9] G. Dougherty and Z. Kawaf, "The point spread function revisited: image restoration using 2-d deconvolution," *Radiography*, vol. 7, pp. 255–262, 2001.
- [10] R. Neelamani, H. Choi, and R. Baraniuk, "ForWaRD: Fourier-wavelet regularized deconvolution for ill-conditioned systems," *IEEE Transactions on Signal Processing*, vol. 52, pp. 418–433, 2004.
- [11] Z. Zhou, F. Gao, H. Zhao, and L. Zhang, "Application of Fourier-wavelet regularized deconvolution for improving image quality of free space propagation x-ray phase contrast imaging," *Physics in Medicine and Biology*, vol. 57, p. 7459, 2012.
- [12] W. H. Richardson, "Bayesian-based iterative method of image restoration," *Journal of the Optical Society of America*, vol. 62, pp. 55–59, 1972.
- [13] L. B. Lucy, "An iterative technique for the rectification of observed distributions," *The Astronomical Journal*, vol. 79, pp. 745–754, 1974.
- [14] J. Verbeeck and G. Bertoni, "Deconvolution of core electron energy loss spectra," *Ultramicroscopy*, vol. 109, pp. 1343–1352, 2009.
- [15] N. Dey, L. Blanc-Feraud, C. Zimmer, P. Roux, Z. Kam, J.-C. Olivo-Marin, and J. Zerubia, "Richardson-Lucy algorithm with total variation regularization for 3D confocal microscope deconvolution," *Microscopy research and technique*, vol. 69, pp. 260–266, 2006.
- [16] K. Ocheltree and L. Frizzell, "Sound field calculation for rectangular sources," *IEEE Transactions on Ultrasonics, Ferroelectrics, and Frequency Control*, vol. 36, pp. 242–248, 1989.
- [17] C. Huygens, *Dioptrica*, Leiden, 1703.
- [18] J. Jensen, "A model for the propagation and scattering of ultrasound in tissue," *Journal of the Acoustical Society of America*, vol. 89, pp. 182–190, 1990.
- [19] C. Bouwkamp, "Diffraction theory," *Reports on Progress in Physics*, vol. 17, pp. 35–100, 1954.
- [20] A. Sommerfeld, "Die frei schwingende Kolbenmembran," *Annalen der Physik*, vol. 42, pp. 389–420, 1943.
- [21] T. Mellow and L. Kärkkäinen, "On the sound field of an oscillating disk in a finite open and closed circular baffle," *The Journal of the Acoustical Society of America*, vol. 118, pp. 1311–1325, 2005.
- [22] K. Li and H. Wong, "A review of commonly used analytical and empirical formulae for predicting sound diffracted by a thin screen," *Applied Acoustics*, vol. 66, pp. 45–76, 2005.
- [23] A. Pierce, *Acoustics - An Introduction to Its Physical Principles and Applications*, 2nd ed. Acoustical Society of America, 1989.
- [24] G. Harris, "Review of transient field theory for a baffled planar piston," *Journal of the Acoustical Society of America*, vol. 70, pp. 10–20, 1981.
- [25] J. Kelly and R. McGough, "A time-space decomposition method for calculating the nearfield pressure generated by a pulsed circular piston," *IEEE Transactions on Ultrasonics, Ferroelectrics, and Frequency Control*, vol. 53, pp. 1150–1159, 2006.
- [26] A. Schoch, "Betrachtungen über das Schallfeld einer Kolbenmembran," *Akustische Zeitschrift*, vol. 6, pp. 318–326, 1941.
- [27] L. V. King, "On the acoustic radiation field of the piezo-electric oscillator and the effect of viscosity on transmission," *Canadian Journal of Research*, vol. 11, pp. 135–155, 1934.
- [28] F. Oberhettinger, "The sound field of a vibrating disk," *Zeitschrift für angewandte Mathematik und Physik ZAMP*, vol. 26, pp. 171–176, 1975.
- [29] J. A. ArcherHall, A. I. Bashter, and A. J. Hazelwood, "A means for computing the Kirchhoff surface integral for a disk radiator as a single integral with fixed limits," *The Journal of the Acoustical Society of America*, vol. 65, pp. 1568–1570, 1979.
- [30] D. A. Hutchins, H. D. Mair, P. A. Puhach, and A. J. Osei, "Continuouswave pressure fields of ultrasonic transducers," *The Journal of the Acoustical Society of America*, vol. 80, pp. 1–12, 1986.
- [31] R. J. McGough, T. V. Samulski, and J. F. Kelly, "An efficient grid sectoring method for calculations of the near-field pressure generated by a circular piston," *The Journal of the Acoustical Society of America*, vol. 115, pp. 1942–1954, 2004.

- [32] M. Abramowitz and I. Stegun, *Pocketbook of mathematical functions*. Harri Deutsch, 1984.
- [33] N. Dey, L. Blanc-Féraud, C. Zimmer, P. Roux, Z. Kam, J.-C. Olivo-Marin, and J. Zerubia, "3D microscopy deconvolution using Richardson-Lucy algorithm with total variation regularization," INRI, Tech. Rep. 5272, 2004.
- [34] J. Starck, E. Pantin, and F. Murtagh, "Deconvolution in astronomy: A review," *Publications of the Astronomical Society of the Pacific*, vol. 114, pp. 1051-1069, 2002.
- [35] M. Laasmaa, M. Vendelin, and P. Peterson, "Application of regularized Richardson-Lucy algorithm for deconvolution of confocal microscopy images," *Journal of Microscopy*, pp. 124-140, 2011.
- [36] K. Moreland, "Diverging color maps for scientific visualization," in *Proceedings of the 5th International Symposium on Visual Computing*, 2009, pp. 92-103.
- [37] D. S. Biggs and M. Andrews, "Acceleration of iterative image restoration algorithms," *Applied Optics*, vol. 36, pp. 1766-1775, 1997.
- [38] R. Zanella, G. Zanghirati, R. Cavicchioli, L. Zanni, P. Boccacci, M. Bertero, and G. Vicidomini, "Towards real-time image deconvolution: application to confocal and STED microscopy," *Scientific Reports*, vol. 3, 2013.
- [39] L. Schmerr and S. Song, *Ultrasonic Nondestructive Evaluation Systems*. Springer, 2007.